Performance degradation of superlattice MOSFETs due to scattering in the contacts

Pengyu Long, Jun Z. Huang, Zhengping Jiang, Gerhard Klimeck, Mark J. W. Rodwell, and Michael Povolotskyi

Citation: Journal of Applied Physics **120**, 224501 (2016); doi: 10.1063/1.4971341
View online: https://doi.org/10.1063/1.4971341
View Table of Contents: http://aip.scitation.org/toc/jap/120/22
Published by the American Institute of Physics

Articles you may be interested in

Negative capacitance in optically sensitive metal-insulator-semiconductor-metal structures
Journal of Applied Physics **120**, 224502 (2016); 10.1063/1.4971401

Junctionless nanowire TFET with built-in N-P-N bipolar action: Physics and operational principle
Journal of Applied Physics **120**, 225702 (2016); 10.1063/1.4971345

S2DS: Physics-based compact model for circuit simulation of two-dimensional semiconductor devices including non-idealities
Journal of Applied Physics **120**, 224503 (2016); 10.1063/1.4971404

Strain effects on thermal transport and anisotropy in thin-films of Si and Ge
Journal of Applied Physics **120**, 225104 (2016); 10.1063/1.4971269

Methods for modeling non-equilibrium degenerate statistics and quantum-confined scattering in 3D ensemble Monte Carlo transport simulations
Journal of Applied Physics **120**, 224301 (2016); 10.1063/1.4970913

InGaAs tunnel FET with sub-nanometer EOT and sub-60 mV/dec sub-threshold swing at room temperature
Applied Physics Letters **109**, 243502 (2016); 10.1063/1.4971830

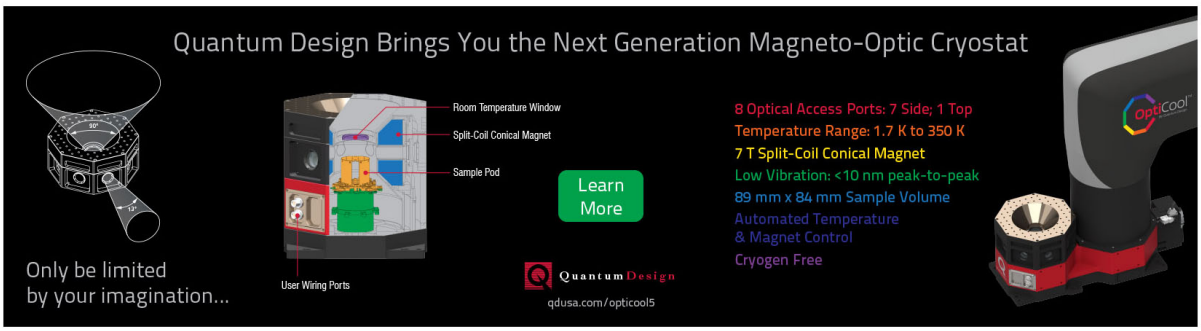

Performance degradation of superlattice MOSFETs due to scattering in the contacts

Pengyu Long,[1] Jun Z. Huang,[1] Zhengping Jiang,[1] Gerhard Klimeck,[1] Mark J. W. Rodwell,[2] and Michael Povolotskyi[1]
[1]*School of Electrical and Computer Engineering, Network for Computational Nanotechnology, Purdue University, West Lafayette, Indiana 47907, USA*
[2]*Department of Electrical and Computer Engineering, University of California, Santa Barbara, California 93106, USA*

(Received 22 September 2016; accepted 19 November 2016; published online 8 December 2016)

Ideal, completely coherent quantum transport calculations had predicted that superlattice MOSFETs (SL-MOSFET) may offer steep subthreshold swing performance below 60 mV/dec to around 39 mV/dec. However, the high carrier density in the superlattice source suggests that scattering may significantly degrade the ideal device performance. Such effects of electron scattering and decoherence in the contacts of SL-MOSFETs are examined through a multi-scale quantum transport model developed in NEMO5. This model couples the NEGF-based quantum ballistic transport in the channel to a quantum mechanical density of states dominated reservoir, which is thermalized through strong scattering with local quasi-Fermi levels determined by drift-diffusion transport. The simulations show that scattering increases the electron transmission in the nominally forbidden minigap, therefore, degrading the subthreshold swing (*S.S.*) and the ON/OFF DC current ratio. This degradation varies with both the scattering rate and the length of the scattering dominated regions. Different SL-MOSFET designs are explored to mitigate the effects of such deleterious scattering. Specifically, shortening the spacer region between the superlattice and the channel from 3.5 nm to 0 nm improves the simulated *S.S.* from 51 mV/dec. to 40 mV/dec. *Published by AIP Publishing.* [http://dx.doi.org/10.1063/1.4971341]

I. INTRODUCTION

Very-large-scale integration (VLSI) devices require low switching energy ($CV_{DD}^2/2$), low OFF-current (I_{OFF}), and large ON-current (I_{ON}) for the desired small delay (CV_{DD}/I_{ON}). "Simple" supply voltage V_{DD} reduction has dominated the development in Moore's law device scaling to reduce the dynamic power consumption. However, simple V_{DD} reduction increases the OFF current of the devices exponentially and today's devices consume as much power when they are switched or when they hold their state.[1] With the fundamental limit of the turn-on slope of the best possible MOSFET is 60 mV/dec voltage, scaling has come to an impasse. Transistors having a subthreshold swing (*S.S.*)[2] smaller than the 60 mV/dec limit of conventional MOSFETs have therefore attracted great interests. In tunnel FETs, the source valence band filters the injected electron energy distribution, reducing the *S.S.*; unfortunately, I_{ON} is reduced by the low PN junction tunneling probability.[3] In superlattice MOSFETs (SL-MOSFETs),[4] the source superlattice minigap similarly filters the injected electron energy distribution, again reducing the *S.S.*; because the transmission within the superlattice miniband can approach 100%, I_{ON} can, in principle be large, approaching that of the conventional MOSFETs.

Reported simulations of SL-MOSFETs predicted appealing device performances with SS values ranging from 10 to 39 mV/dec (Refs. 4–6) using coherent quantum transport models. In these models, electrons travel through a quantum mechanical defined miniband coherently, even though the superlattice-shaped source contains a very high carrier density of the order of 10^{18}–10^{19}/cm^3. With such high carrier densities, it must be assumed that carrier scattering and decoherence effects must be present possibly degrading the perceived advantages of the superlattice injector. Electron-phonon scattering has been shown to reduce the drain current in conventional nanowire MOSFETs.[7] In SL-MOSFETs, strong scattering in the contacts may also drive electrons towards a thermal energy distribution,[8] degrading the superlattice energy-filtering functionality and thereby increasing the S.S. and I_{OFF}. To assess the potential application of SL-MOSFETs in future VLSI circuits, the effect of scattering should, therefore, be studied to gauge the technical viability of these complex new SL-MOSFETs.

The self-consistent Born approximation (SCBA) within non-equilibrium Green's function (NEGF) method[9] treats individual scattering processes explicitly. Scattering interactions with various phonons, interface roughness, and alloy disorder have been shown to be strong in resonant tunneling diodes only at low temperature.[9,11] However, the explicit treatment of strong, close to thermalizing electron-electron scattering with an explicit NEGF self-energy has been elusive. Moreover, the method is one or two orders of magnitude more computationally intensive than the ballistic simulations.[7] Thermalizing scattering in quantized and continuum injector states in resonant tunneling diodes has, however, been shown to be critical to the quantitative device modeling and prediction.[10,11] This generalized treatment of complex states occupied by a thermalized carrier distribution

has been implemented in 1D, 2D, and 3D geometries in NEMO5. The single scattering rate embedded in the generalized contact method represents the effects of multiple scattering mechanisms[12] and can be directly related to experimentally relevant parameters such as the mean free path and momentum relaxation time. This thermalized contact treatment requires the computation of the diagonal elements of the contact Green function using the Recursive Green Function (RGF) algorithm. The thermalized contacts have well-established quasi-Fermi levels determined by solving the drift-diffusion equation[13,14] in them. For 2D and 3D devices, this approach is only about five times slower than the ballistic Quantum Transmitting Boundary Method (QTBM),[15] which, cannot handle such complex, scattering influenced contacts.

This paper first briefly introduces the phenomenological scattering model, and then applies it to study the effects of scattering on the OFF-state (thermalization and broadening) and ON-state characteristics of the SL-MOSFETs. The effect of spacer on the OFF-state performance and how it can be designed to improve the device S.S are discussed.

II. DEVICE STRUCTURE AND THE MODELING METHOD

The double-gate ultra-thin-body (UTB) SL-MOSFET considered here is an $In_{0.53}Ga_{0.47}As$ channel MOSFET with an $In_{0.53}Ga_{0.47}As/In_{0.52}Al_{0.48}As$ superlattice embedded in its source region. The device structure is illustrated in Fig. 1, with its optimized design parameters listed in Table I.

The device is simulated using the atomistic nanoelectronics modeling toolset NEMO5[16,17] by self-consistently solving Poisson's equation and a set of multi-scale transport equations. In the multi-scale transport approach, the phenomenological scattering model is applied to the source thermalized reservoir, where the carrier energy levels are broadened, and imposed in the drain thermalized reservoir, where carriers dissipate their remaining kinetic energy after ballistic transmission through the central non-equilibrium device. Scattering is neglected in the channel. The separation of scattering free and strong scattering device regions is supported by simulations which showed that the scattering rate

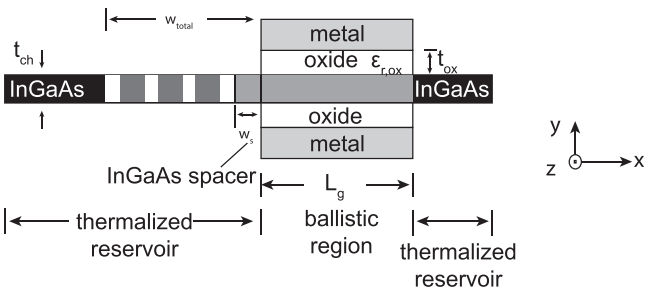

FIG. 1. Device geometry of the SL-MOSFET. The channel length (thickness) is L_g (t_{ch}). The gate oxide thickness is t_{ox}, with a dielectric constant ε_r. The source (drain) doping density is N_S (N_D). The superlattice consists of multiple quantum wells ($In_{0.53}Ga_{0.47}As$) and barriers ($In_{0.52}Al_{0.48}As$) with lengths denoted by w_i and b_i. The well doping is N_w. The spacer between the superlattice and the channel has a length denoted by w_s. The structure extends infinitely in the z-direction (perpendicular to the page).

TABLE I. Device parameters of the SL-MOSFET shown in Fig. 1. Unit ml denotes monolayers.

Parameter	Value	Parameter	Value (ml)
t_{ox}	2.56 nm	b_1	4
ε_r	20	w_1	12
t_{ch}	3.2 nm	b_2	6
L_g	20 nm	w_2	12
$N_{S,D}$	2.5×10^{19} cm^{-3}	b_3	6
N_w	1×10^{19} cm^{-3}	w_3	12
w_s	3.5 nm	b_4	4
w_{total}	20 nm	w_s	12

in the channel is more than one order of magnitude smaller than that in the contacts.[18]

A full non-equilibrium quantum statistical mechanics solution of the transport problem including all relevant particle-particle interactions is in principle possible with the NEGF (Non-Equilibrium Green's Function) formalism. Electron interactions with phonons, interface roughness, or alloy disorder have been treated within NEGF approach in a physically predictive way.[19] Electron-electron scattering, however, is in principle non-local in physical space and energy/momentum space resulting in completely full matrices, which are too large to be solved/inverted for realistically extended devices. No "exact" and practical approach to e-e scattering in NEGF is known at this time. e-e interactions combined with all the other scattering mechanisms are however critically important in the thermalization process in high electron density device regions. Efforts to model the high-intensity scattering in high electron densities have in principle failed to properly treat the close-to-thermalized electron occupancy in devices such as the resonant tunneling diodes, resulting in unphysical descriptions/prediction of bi-stability in devices.[8,20] Rather than spending immense amounts of computational resources to obtain a very-close-to equilibrium distribution with a full NEGF approach, it is much more strategic and practical to impose local thermal equilibrium on a quantum mechanically defined density of states.[10] Such an approach subdivides the device into multiple regions whose electron occupancy is dramatically different. The source and drain with their very large carrier densities are assumed to be in a local thermal equilibrium, while the central device which is typically tunneling or coherent transport dominated can be treated in non-equilibrium. The equilibrium reservoirs are thermalized with a scattering rate. A physics based scattering rate should in principle be dependent on the distribution of electrons in energy, momentum, and space. Such space, energy, and momentum dependent scattering rates can in principle be computed, but add significant complexity. As a first implementation in NEMO5, we have chosen a scattering rate model that is rather simple: a) constant in energy above the transverse momentum dependent band edge and exponentially decaying under that band edge. The scattering potential is gleaned from experimentally observed scattering rates. We emphasize here that the extended states in the source, not just the local DOS at the end of the source are critical to the injection into the channel.

To summarize the phenomenological scattering model, in the thermalized reservoirs, an energy and momentum dependent imaginary potential $i\eta$ are added to the on-site elements of the reservoir Hamiltonian to account for the scattering-induced broadening:

$$[G^R(k_z,E)^{-1}]_{r,r} = E - H(k_z)_{r,r} - qV_{r,r} + i\eta(k_z,E)_{r,r}, \quad (1)$$

where $\eta(k_z,E)_{r,r} = \eta_0$ if $E > E_c(r,k_z)$, and $\eta(k_z,E)_{r,r} = \eta_0 \exp\left[\frac{E-E_c(r,k_z)}{\eta_0}\right]$ if $E \le E_c(r,k_z)$, with E_c being the conduction band edge, $[G^R]^{-1}{}_{r,r}$ represents the on-site elements of the inverse of the Green's function at position r, k_z is the transverse wave vector, E is the energy, $H_{r,r}$ is the diagonal element of the Hamiltonian, $V_{r,r}$ is the potential at position r and $i\eta$ is a small imaginary potential related to the scattering rate. The recursive Green's function (RGF) algorithm[21] is used to obtain in a targeted fashion only the needed matrix elements of the inverted matrix efficiently.[9]

The electrons in the reservoirs are assumed to be in equilibrium with the local quasi-Fermi levels, given by

$$n_r^{res} = \int \frac{dk_z}{2\pi} \int \frac{dE}{2\pi} A(k_z,E)_{r,r} f_{FD}(E - E_{Fr}), \quad (2)$$

where f_{FD} is the Fermi-Dirac distribution function, E_{Fr} is the local quasi-Fermi level, and $A_{r,r}$ is the E and k_z dependent spectral function in the reservoirs

$$A(k_z,E)_{r,r} = i[G^R(k_z,E)_{r,r} - G^R(k_z,E)^+{}_{r,r}]. \quad (3)$$

The quasi-Fermi levels E_{Fr} are determined by solving the continuity equation in the reservoirs

$$\nabla \cdot J_r = 0, \quad (4)$$

where $J_r = \mu n_r \nabla E_{Fr}$ is the total drift-diffusion current density in the reservoirs, with μ being the carrier mobility and n_r given in (2). Boundary condition $E_{Fr} = E_{FS}$ (E_{FD}) is employed at the left (right) edge of the source (drain) reservoir, where E_{FS} (E_{FD}) is the Fermi level of the source (drain) contact. We emphasize here that this form of the drift-diffusion equation can contain complex, quantum mechanically defined local charge densities. The current continuity throughout the whole device is established by enforcing the current at the reservoir-channel interfaces to be equal to the ballistic current of the central region[13]

$$I_{LR} = \frac{q}{h} \int \frac{dk_z}{2\pi} \int \frac{dE}{2\pi} T(k_z,E)[f_{FD}(E - E_{FL}) - f_{FD}(E - E_{FR})], \quad (5)$$

where T is E and k_z dependent transmission coefficient, E_{FL} and E_{FR} are the quasi-Fermi levels at the left and right boundaries of the channel region, q is the electron charge, and h is the Planck constant. The transmission is calculated at the boundary of the thermalized reservoir and channel. As the RGF algorithm have marched through the entire device, both the effects of both reservoir and channel have been captured. More details of this generalized boundary condition method can be found in IV A. of 9

A Newton solver is developed to solve the nonlinear equation (4). Once the quasi-Fermi levels are determined, the electron density distribution in the reservoirs is obtained by (2) and the density distribution in the channel is obtained by

$$n_r^{ch} = \int \frac{dk_z}{2\pi} \int \frac{dE}{2\pi} [A_L(k_z,E)_{r,r} f_{FD}(E - E_{FL}) + A_R(k_z,E)_{r,r} f_{FD}(E - E_{FR})], \quad (6)$$

where A_L and A_R are the left-connected and right-connected spectral functions in the channel.[22] Figure 2 depicts the process for the self-consistent solution to the Poisson equation with the multi-scale transport.

The simulations use scattering potentials η of 5 meV and 10 meV, corresponding to scattering time τ of 66 fs and 33 fs, respectively, according to $\tau = \hbar/(2\eta)$,[23] are similar to values from the literature.[24] Khondker *et al.*[25] considered the phonon and random impurity scattering and concluded that when the resonant states are filled, τ is approximately 80 fs. Given a $\sim 1.5 \times 10^7$ cm/s thermal velocity v_{th}, the mean free path $\lambda = v_{th}\tau$ is 10.5 nm for $\eta = 5$ meV and is 5.3 nm for $\eta = 10$ meV. From $\mu = q\tau/m^*$, where m* is the electron effective mass of confined $In_{0.53}Ga_{0.47}As$. $\eta = 5$ meV corresponds to μ of 1206 $cm^2/(V \cdot s)$, and 10 meV corresponds to 603 $cm^2/(V \cdot s)$.

III. DISCUSSION

The effect of scattering in the reservoirs on the transmission probability through the central device is studied by varying the imaginary scattering potential. The transistor off-state is defined with $V_{DS} = 0.2$ V, $V_{GS} = 0$ V, and with the threshold voltage adjusted so that the off-state current, given zero scattering, is 0.1 A/m. The transistor ON-state is defined with $V_{DS} = V_{GS} = 0.2$ V.

Fig. 3 shows the band diagram, transmission, and energy-resolved current density for the ON- and OFF-states (top and bottom row, respectively). The effect of scattering in the source is examined by ramping the empirical

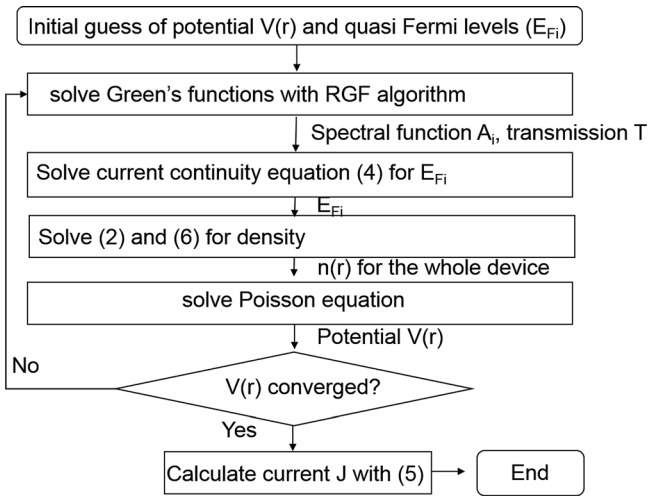

FIG. 2. Flowchart of the multi-scale transport simulation with ballistic transport in the channel and phenomenological scattering model in the reservoirs.

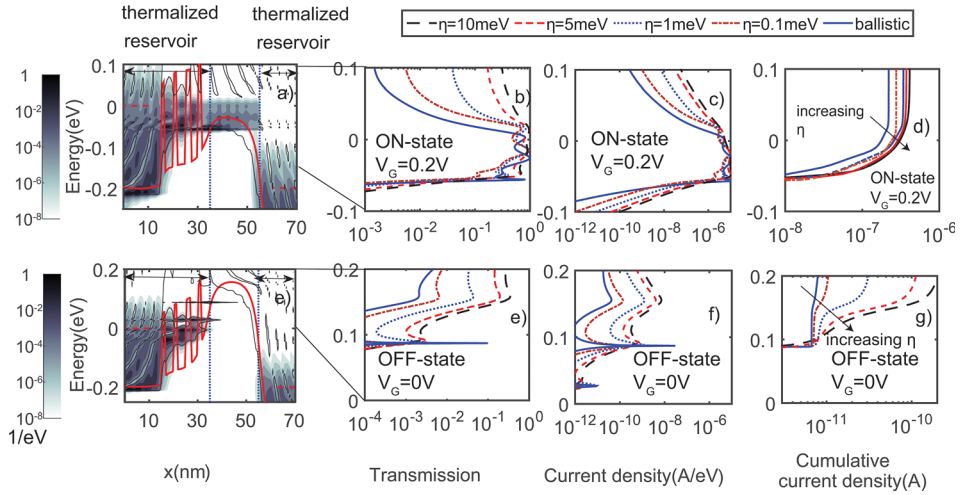

FIG. 3. (a) Energy band diagram and electron density profile of the SL-MOSFET in an ON-state bias with the scattering and ballistic regions indicated; (b) transmission probability versus energy given a zero transverse wave vector k_z; (c) energy-resolved current density $J(E)$ (d) cumulative current density for $k_z = 0$. As η increases, the transmission in the off-resonant minigap increased exponentially, and the resonant states are broadened. In ON current increases slightly by about a factor of 2 due to the broadening inside the miniband. (e)–(h) plot the energy band diagram, transmission, energy-resolved current, cumulative current in an OFF-state state bias. In plots (b)–(h), imaginary scattering potentials η of 0.1 meV, 1 meV, 5 meV, and 10 meV are applied. As η increases, the transmission in the off-resonant minigap increased exponentially, and the resonant states are broadened. The OFF current increases by a factor of 25×. The gate voltage is NOT scaled for I_{OFF} normalization.

scattering potential from 0.1 meV to 10 meV. ON and OFF current shows different sensitivities to the increased rate of scattering in the source.

Fig. 3(a) depicts the local density of states superposed with the local charge density, in addition to the band edges and the Fermi Levels in the ON state. The injection of carriers from the superlattice emitter into the channel region is clearly visible. The electrons travel ballistically through the channel region and are, by the model assumption, rapidly thermalized in the collector/drain.

Fig. 3(b) zooms into the energy range where the miniband injection occurs and plots the transmission coefficient. As the empirical scattering rate is increased, the energetic definition of the miniband is softened, and the ripples in the transmission window are broadened. Fig. 3(c) plots the corresponding energy dependent current density. Given the high bias between the source and drain, this current density is basically the transmission in Fig. 3(b) multiplied by the Fermi function in the injection site. Due to the exponential decay of the Fermi function, the dramatic exponential broadening of the transmission is counteracted. From Fig. 3(c), however, it is hard to tell if the current will increase or decrease. It is instructive to define the following quantity which we entitle as the "running integral of the current density". This integral converts the resonance dominated current channels into step-like contributions to the total current

$$J_{int}(E,k) = \int_{E_0}^{E} dE'\, J(E',k),$$

where E_0 represents the lower energy limit and E1 the upper energy limit.

Fig. 3(d) shows the counter-intuitive result that the ON-current increases slightly as the scattering strength is increased. The overall current is increased by an 86% as eta is increased to a maximum value of 10 meV. In the ON state, both with weak and strong scattering, current is primarily carried by the superlattice miniband. Scattering causes an increased coupling between the individual quantum wells and in overall broadens the remaining resonance features and couples them more strongly in energy. The peak resonance transmissions are reduced, however, the broadening increases the total transmission across the miniband energy range significantly.

The lower row of Fig. 3 compares the OFF state behavior to the top row ON state behavior. In the OFF state, the miniband is nominally blocked by the gate potential and remains reasonably unaffected by the scattering strength. The off-resonance transmission *above* the miniband, however, is significantly increased with increased scattering strength as clearly visible in Fig. 3(e). The current density panel in Fig. 3(f) shows that there is indeed a significant current flowing at high energies, above the miniband. The cumulative current density in Fig. 3(g) shows clearly that the OFF current increases by a factor of 25.

The simulation results in Figure 3 have NOT been shifted in voltage such that I_{OFF} is normalized to 0.1 A/m to examine the physical effects of scattering on the detailed states in the superlattice and their effect of carrier injection into the channel. In these examination conditions, the ON-current increases slightly (86%) and the OFF-current increases by a factor of 25. If the I–V curves were voltage-shifted to $I_{OFF} = 0.1$ A/m, then the ON-current would appear to be significantly reduced due to scattering, which in turn is a more expected result.

Another effect of scattering in the emitter is a resistive transport behavior, which results in a Fermi level drop, and a self-consistent deformation of the semiconductor band edge. A Fermi level and potential drop in the source, in turn, change the superlattice alignment and change the injection into the central device. Sophisticated drift-diffusion models

with various scattering mechanisms are available today in commercial simulators[26–28] for standard semiconductor devices. These simulators in general do not handle heterostructures within a quantum mechanical approach that details a spatial, and energy and momentum dependent scattering. Mobility models for such heterostructures are subject to commercial development. Here we are limited to the empirical exploration of simple mobility models that involve an "exact" density of states.

In reality, the mobility is related to the mean free time and thus the scattering rate. To reflect this relation, the mobility in the rest of this paper will be determined from $\mu = q\tau/m^*$, where m* is the electron effective mass of confined $In_{0.53}Ga_{0.47}As$. The mean relaxation time is defined as $\tau = \hbar/(2\eta)$. $\eta = 5$ meV that corresponds to μ of 1206 $cm^2/(V{\cdot}s)$, and 10 meV corresponds to 603 $cm^2/(V{\cdot}s)$.

Fig. 4 shows the I_D-V_G characteristics with the threshold now adjusted to normalize I_{OFF} to 0.1 A/m for all devices. The S.S. (Fig. 4(a)) degrades from 39 mV/dec. in the ballistic case to 51 mV/dec at $\eta = 5$ meV and 60 mV/dec at $\eta = 10$ meV. The ON-current degrades from 360 A/m in the ballistic case to 240 A/m at $\eta = 5$ meV and 180 A/m at $\eta = 10$ meV. The degradation in ON/OFF ratio is partially caused by the increase in OFF-state leakage current and partially caused by the quasi-Fermi level drop in the thermalized reservoirs. For this constant OFF-current, the SL-MOSFETS deliver significantly higher ON/OFF ratios (even with scattering) of values of 3600, 2400, and 1800 over the standard MOSFET with an ON/OFF ratio of 1800 at 0.2 V. With 10 meV intense scattering, the ON/OFF ratio of SL MOSFET approaches that of the MOSFET. The inset in Fig. 4(a) shows the value of the S.S. as a function of gate voltage. On this voltage scale, the region of sub 60 mV/dec is below 0.1 V and a S.S. degradation due to scattering is clearly visible.

Fig. 4(b) shows the same data of Fig. 4(a) without the I_{OFF} normalization. The increase in the OFF current is visible on the exponential scale. On this voltage reference, the ON current is hardly changed by the scattering in the SL-MOSFET.

Figure 5 depicts the effects of scattering in superlattices of different lengths (four and five barriers). The transmission probability is plotted in the transistor ON state, both in the ballistic case and with $\eta = 5$ meV, for superlattices having four and five barriers. In the ballistic case, the off-resonant transmission in the superlattice minigap decreases as the number of superlattice periods is increased (Fig. 5(a)), as expected. The miniband becomes more well-defined.

The 5 meV scattering strength corresponds to a decoherence length of 9.9 nm, the transmission in the superlattice minigap is similar for the four-barrier and five-barrier superlattice designs, and there is little benefit in using more superlattice periods. In fact on this voltage scale here it appears that while the coherent 5 barrier structure delivers a higher current than the 4 barrier structure, the opposite is true when the scattering is present (Fig. 5(d)).

An additional negative effect due to adding more superlattice cells can be understood intuitively in the context of scattering and thermalization. If there is strong thermalization in the superlattice due to the high carrier densities, then adding more cells begins to drop the Fermi level over a longer leverage arm, stretching out the I–V characteristic over a wider range of source-drain biases, thus reducing the ON current by moving the highest possible current out of the voltage of interest below 0.2 V. Indeed this is what Figure 6(a) shows. The Gedanken experiment in Fig. 6 is constructed such that in a nominally unchanged device, the region in which incoherent scattering is enforced is increased from just the left contact to enclose more and more barriers of the superlattice. The voltage scale is not changed between these simulations

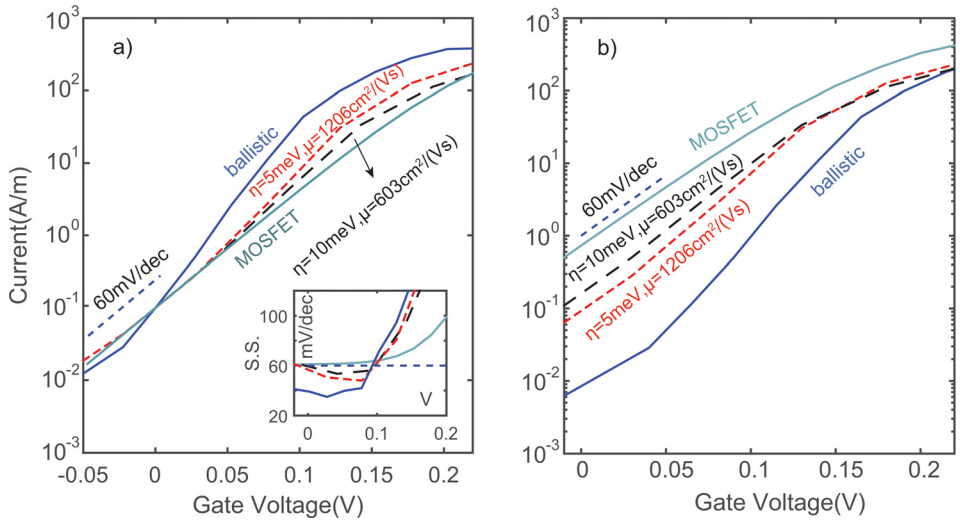

FIG. 4. Comparison of the transfer characteristics of the ideal ballistic SL-MOSFET, SL-MOSFET with two different scattering potentials (in units of meV) and mobilities (in units of cm^2/V s), and a conventional MOSFET with identical structure except for the superlattice. (a) I-V data is aligned at the same I_{OFF} of 0.1 A/m by adjusting the metal workfunction of the gate. The ideal SL-MOSFET delivers an ON/OFF ratio of 3600 at 0.2 V, while the MOSFET has a ratio of 1800. Scattering in the superlattice reduces the ON/OFF ratio to 2400 and 1800 for the two different scattering strengths, 10 meV scattering case approaches the limit of the MOSFET. The inset of (a) plots the subthreshold swing (S.S.) for the four simulations as a function of gate voltage. A degradation in S.S. due to scattering is clearly visible. (b) Without adjusting the metal workfunction (no I_{OFF} normalization). The simulations predict an exponential increase in I_{OFF} and degraded S.S. with the introduction of scattering.

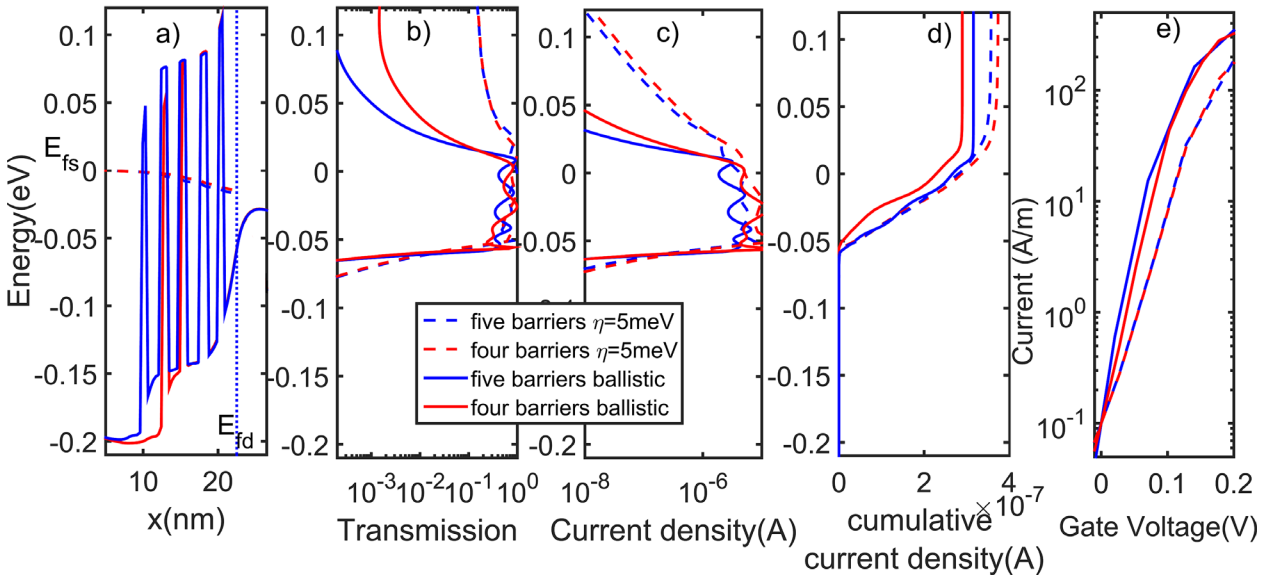

FIG. 5. Exploration of two different superlattice lengths with four and five barriers. (a) Band diagrams and quasi-Fermi levels at ON-state. (b)–(d) Corresponding transmission probabilities, energy resolved current, cumulative current for superlattices with four and five barriers, in the ballistic limit and with scattering in the contacts ($\eta = 5$ meV, $\mu = 1206\,\mathrm{cm^2/V\,s}$). Fig. 5(e) shows the ballistic and scattering transfer characteristics of four and five barrier superlattices. In the ballistic transport case, the addition of barriers refines the transmission through the miniband as expected. However, broadening due to incoherent scattering counteracts the definition of the minibands and raises the non-resonant band tails, which ultimately increases the OFF current and results in similar S.S. with four and five barrier superlattices. The gate voltage is NOT scaled for I_{OFF} normalization.

(no normalization of I_{OFF}). As the number of superlattice periods increases, the quasi-Fermi levels decrease more in the thermalized reservoirs, which affects the ON-state current. Therefore, the modeling of incoherent scattering leads to critical device design insight and in this case, simplifies the overall design of the device as only a limited number of barriers are needed.

The modeling with NEMO5 can also address the critical issue to determine the region in which scattering has the most detrimental effect. Fig. 6(c) shows the energy-dependent superlattice transmission as a function of the extent of the region in which thermalizing scattering is imposed. The superlattice energy filtering is most rapidly degraded by scattering immediately adjacent to the channel (in the spacer); electrons that are only scattered close to the source will still have steep energy-dependent filtering as they pass through the remainder of the superlattice.

The critical dependence on the extent of the scattering region, or from a different point of view, the strong dependence of the transport on the few nanometers close to the

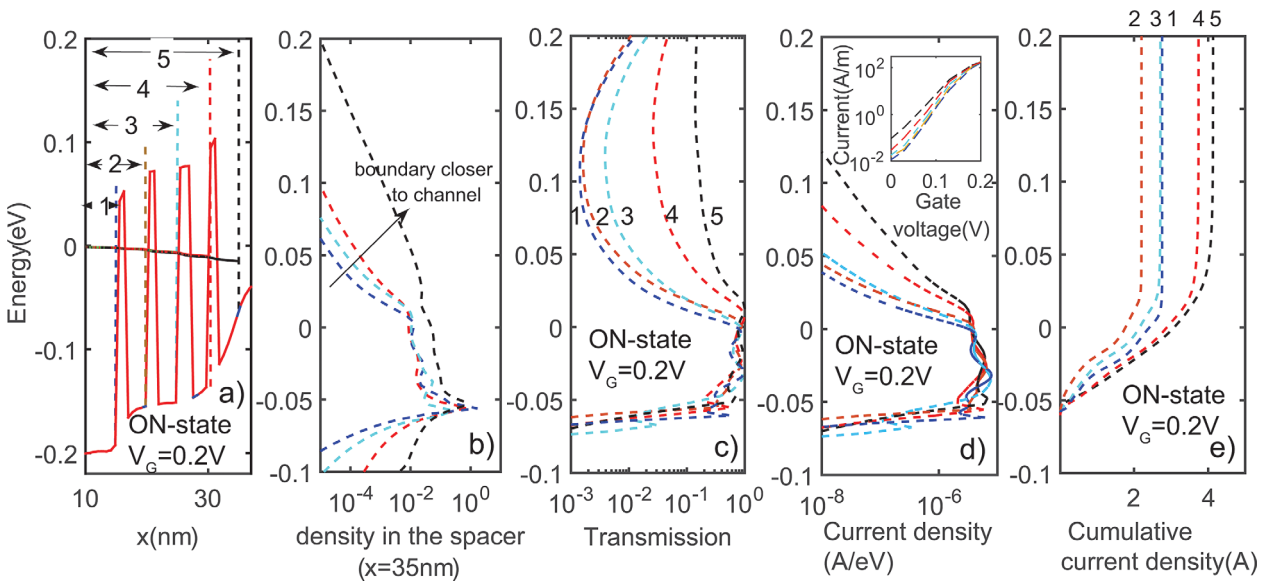

FIG. 6. Energy-resolved dependence analysis of the extent of the reservoir treatment. (a) Band edge diagram in the ON-state at 0.2 V for the completely ballistic device. (b) Electron density closely in front of the channel (x = 35 nm) (b), transmission probability (c), energy resolved current (d), cumulative current density (e) for different regions where scattering takes place (a) for a four-barrier superlattice. $\eta = 5$ meV, $\mu = 1206\,\mathrm{cm^2/V\,s}$ is assumed in the indicated regions (1 through 5) and in the drain, with ballistic transport assumed in the rest of the transport path. Inset in Fig. 6(d) shows the transfer characteristics with different boundaries. The superlattice energy filtering is most rapidly degraded by scattering immediately adjacent to the channel (in the spacer). The gate voltage is NOT scaled for I_{OFF} normalization.

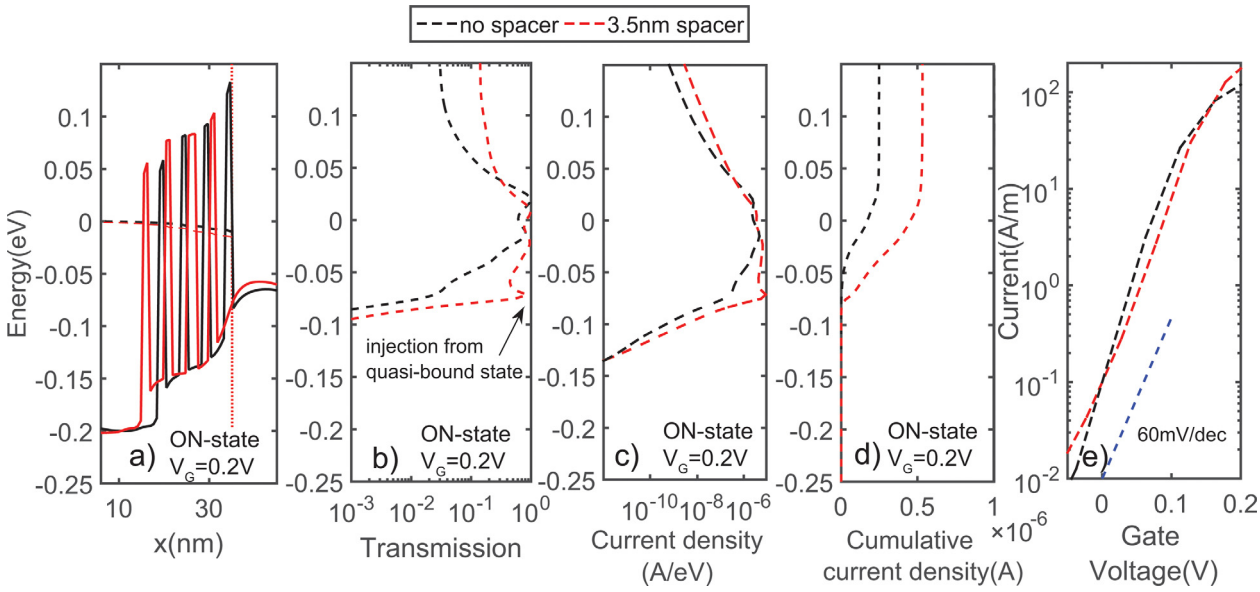

FIG. 7. Exploration of an optimized design that avoids the spacer between the superlattice and the channel assuming $\eta = 5$ meV, $\mu = 1206\,\mathrm{cm^2/V\ s}$ in the source in ON state. (a) energy band diagrams including a 3.5 nm spacer (red line) and without a spacer between the superlattice and the channel (black line); (b) transmission (c) energy resolved current density (d) cumulative current. As the spacer layer is reduced and the superlattice pushed closer to the gate the injection from quasi-bound state diminished, the total current decreased. (e) I_{DS}-V_{GS} characteristics at $V_{DS} = 0.3$ V, computed with $\eta = 5$ meV, for a 3.5 nm spacer and no spacer between the superlattice and the channel. in (e) The gate voltage is adjusted to set the OFF current to 0.1 A/m.

channel is also illustrated in Fig. 6(b). If the boundary is set close to the source (boundary 1 in Fig. 6(a), transport through the superlattice and channel is ballistic, the electron density is well confined to the energy range of miniband (Fig. 6(b)). If the boundary is set to left of the channel (boundary 5 in Fig. 6(a)), the electron density above and below the miniband increased (Fig. 6(b)). The increase in density is because (1) electrons re-thermalized after crossing the superlattice region, counterweighing the effects of energy filter; (2) the quasi-bound state in the spacer (x = 35 nm) is broadened. This change in density causes the superlattice miniband to move up slightly in energy, as shown in Fig. 6(c).

The simulations of Fig. 6 indicate that the superlattice FET subthreshold swing and the OFF-current are strongly degraded by scattering in the region between the superlattice and the channel potential barrier. To investigate this, the energy-dependent transport characteristics, and current-voltage characteristics are simulated comparing a case with spacer and without, both under the condition of $\eta = 5$ meV, $\mu = 1206\,\mathrm{cm^2/(V\ s)}$. The voltage scales are scaled to normalize I_{OFF}. As the spacer is removed, the transmission in the superlattice minigap becomes smaller (Fig. 7(b)) and the device I_D-V_{GS} characteristics become steeper (Fig. 7(e)). The subthreshold swing improves from 51 mV/dec. with $w_s = 3.5$ nm to 40 mV/dec. with $w_s = 0$ nm.

As the spacer is removed, the potential profile within the superlattice is more strongly modulated by the gate potential (Fig. 7(a)). This modulation misaligns the states within the superlattice, perturbing the ON-state transmission characteristics (Fig. 7(b)). In addition, the injection from the quasi-bound state (inside the spacer) is also removed, causing I_{ON} to decrease (Fig. 7(e)) (under a condition of constant I_{OFF}). This somewhat counter-intuitive result displays the critical interplay of the incoherent effects in the injector superlattice and the transport through the central device region. Addressing these incoherent effects are critical to predicting and understanding the performance of today's steep S.S. transistors.

IV. SUMMARY

Previous work had proposed superlattices to be inserted into the source of a MOSFET to overcome the 60 mV/dec limitation. These model predictions assumed a perfectly coherent transport throughout the device region. In this work, the effect of carrier scattering on the DC characteristics of 2D SL-MOSFETs has been analyzed in detail. This simulation work shows that reasonable assumptions of scattering in the high carrier density superlattice source degrade the device performance from the coherent theoretical limit. Scattering degrades the transistor subthreshold swing (*S.S.*) and the I_{ON}/I_{OFF} current ratio. Given significant scattering, increasing the number of superlattice filter periods does not significantly improve the transistor performances. These model predictions, therefore, simplify the overall device design by a quantitative metric. As the device characteristics are most strongly degraded by scattering in the spacer region immediately before the channel, removing the spacer between the superlattice and the channel improves the subthreshold swing, but at the cost of degrading the ON current.

ACKNOWLEDGMENTS

The use of nanoHUB.org computational resources under NSF Grant Nos. EEC-0228390, EEC-1227110, EEC-0634750, OCI-0438246, OCI-0832623, and OCI-0721680 is gratefully acknowledged. This material is based upon the work supported under the NSF Grant (1509394). NEMO5

developments were critically supported by an NSF Peta-Apps award OCI-0749140 and by Intel Corp.

[1]E. Pop, Nano Res. **3**, 147 (2010).
[2]T. N. Theis and P. M. Solomon, Proc. IEEE **98**, 2005 (2010).
[3]S. O. Koswatta, M. S. Lundstrom, and D. E. Nikonov, IEEE Trans. Electron Devices **56**, 456 (2009).
[4]E. Gnani, P. Maiorano, S. Reggiani, A. Gnudi, and G. Baccarani, IEEE Int. Electron Devices Meet. **2011**, 5.1.1.
[5]P. Maiorano, E. Gnani, A. Gnudi, S. Reggiani, and G. Baccarani, Solid-State Electron. **101**, 70 (2014).
[6]P. Long, M. Povolotskyi, B. Novakovic, T. Kubis, G. Klimeck, and M. J. W. Rodwell, IEEE Electron Device Lett. **35**, 1212 (2014).
[7]M. Luisier and G. Klimeck, Phys. Rev. B **80**, 155430 (2009).
[8]K. L. Jensen and F. A. Buot, Phys. Rev. Lett. **66**, 1078 (1991).
[9]R. Lake, G. Klimeck, R. C. Bowen, and D. Jovanovic, J. Appl. Phys. **81**, 7845 (1997).
[10]G. Klimeck, R. Lake, and S. Datta, Phys. Rev. B **50**, 5484 (1994).
[11]R. C. Bowen *et al.*, J. Appl. Phys. **81**, 3207–3213 (1997).
[12]G. Klimeck, R. Lake, R. C. Bowen, W. R. Frensley, and T. Moise, Appl. Phys. Lett. **67**, 2539 (1995).
[13]G. Klimeck, J. Comput. Electron. **2**, 177 (2003).
[14]C. Yam, J. Peng, Q. Chen, S. Markov, J. Z. Huang, N. Wong, W. C. Chew, and G. H. Chen, Appl. Phys. Lett. **103**, 062109 (2013).
[15]M. Luisier, A. Schenk, W. Fichtner, and G. Klimeck, Phys. Rev. B **74**, 205323 (2006).
[16]J. E. Fonseca, T. Kubis, M. Povolotskyi, B. Novakovic, A. Ajoy, G. Hegde, H. Ilatikhameneh, Z. Jiang, P. Sengupta, Y. Tan *et al.*, J. Comput. Electron. **12**, 592 (2013).
[17]S. Steiger, M. Salmani-Jelodar, D. Areshkin, A. Paul, T. Kubis, M. Povolotskyi, H.-H. Park, and G. Klimeck, Phys. Rev. B **84**, 155204 (2011).
[18]P. Palestri, D. Esseni, S. Eminente, C. Fiegna, E. Sangiorgi, and L. Selmi, IEEE Trans. Electron Devices **52**, 2727 (2005).
[19]D. K. Blanks, G. Klimeck, R. Lake, D. Jovanovic, R. C. Bowen, C. Fernando, W. R. Frensley, and M. Leng, in *Proceedings of the 1997 IEEE International Symposium on Compound Semiconductors* (1997), 639–642.
[20]P. Douglas Yoder, M. Grupen, and R. Kent Smith, IEEE Trans. Electron Devices **57**, 3265 (2010).
[21]J. A. Stovneng and P. Lipavsky, Phys. Rev. B **49**(164) 594 (1994).
[22]S. Datta, *Quantum Transport: Atom to Transistor* (Cambridge University Press, Cambridge, UK; New York, 2005).
[23]A. Wacker, Phys. Rep. **357**, 1 (2002).
[24]J. Chen, G. Chen, C. H. Yang, and R. A. Wilson, J. Appl. Phys. **70**, 3131 (1991).
[25]A. N. Khondker and A. Haque, Phys. Rev. B **55**, 15798 (1997).
[26]Synopsis, Sentaurus Device User Guide, Version F-2011.09 (2011).
[27]Atlas User's Manual: Device Simulation from Silvaco International, Version 5.19.20 (last accessed 2 October 2013).
[28]M. R. Pinto, K. Smith, M. Alam, S. Clark, X. Wang, G. Klimeck, and D. Vasileska, see https://nanohub.org/resources/padre for Padre (2014).